A path integral Monte Carlo (PIMC) method based on Feynman-Kac formula for electrical impedance tomography ☆,☆☆

Cuiyang Ding [a], Yijing Zhou [b], Wei Cai [c], Xuan Zeng [a,*], Changhao Yan [a,*]

[a] *State Key Laboratory of ASIC and System, School of Microelectronics, Fudan University, Shanghai, China*
[b] *Department of Mathematics and Statistics, University of North Carolina at Charlotte, Charlotte, NC 28223, USA*
[c] *Department of Mathematics, Southern Methodist University, Dallas, TX 75275, USA*

ARTICLE INFO

ABSTRACT

A path integral Monte Carlo method (PIMC) based on a Feynman-Kac formula for the Laplace equation with mixed boundary conditions is proposed to solve the forward problem of the electrical impedance tomography (EIT). The forward problem is an important part of iterative algorithms of the inverse EIT problem, and the proposed PIMC provides a local solution to find the potentials and currents on individual electrodes. Improved techniques are proposed to compute with better accuracy both the local time of reflecting Brownian motions (RBMs) and the Feynman-Kac formula for mixed boundary problems of the Laplace equation. Accurate voltage-to-current maps on the electrodes of a model 3-D EIT problem with eight electrodes are obtained by solving a mixed boundary problem with the proposed PIMC method.

1. Introduction

Electrical Impedance Tomography (EIT) is often used as a non-invasive medical imaging technique to image the electrical properties such as the conductivity on a part of the body by surface electrode measurements. Its main advantage is the absence of exposure to radioactive materials, compared with other techniques such as X-rays. Applications of EIT include detection of breast cancer, blood clots, pulmonary emboli, etc. Essentially, through only surface measurements, the internal electric conductivity is identified as an image inside the human body by solving an inverse problem. This is possible as the electric conductivity of malignant tumors, being a high-water-content tissue, is one order higher than that of surrounding normal (fat) tissues, allowing one to identify potential diseases and locations through the constructed image of the body [5]. EIT is also a useful tool in geophysics, environmental sciences, and nondestructive testing of materials. For example, it can be used to locate underground mineral deposits, detect leaks in underground storage tanks and monitor flows of injected

fluids into the earth for the extraction or environmental cleaning. Moreover, EIT has also been used to find the corrosion or defects of construction and machinery parts [5][2] without invasion or destructive testing.

For most of the applications, researchers are faced with the problem of finding out the conductivity inside an object with only partial boundary measurements [1]. This poses a great computational challenge as the conductivity inverse problem is nonlinear, unstable, and intrinsically ill-posed [2]. In theory, complete boundary measurements could determine the conductivity in the interior uniquely [13][29]. However, in practice, only a limited number of electrodes and current patterns are available from measurements to reconstruct the conductivity. Various inversion algorithms have been proposed and fall into two categories, non-iterative and iterative methods. Non-iterative methods often assume that the conductivity is close to a constant. In [4], Calderón proved that a map between the conductivity function γ and a quadratic energy functional Q_γ is injective when γ is in a sufficiently small neighborhood of a constant function, and an approximation formula was given to reconstruct the conductivity. Among the iterative approaches, the back-projection method of Barber-Brown [24] gave a crude approximation to the conductivity increment $\delta\gamma$ based on the inverse of the generalized Radon transform, which works best for smooth $\delta\gamma$ or $\delta\gamma$ whose singularity is far from the boundary. For multiple electrode systems, Noser algorithm [5] minimizes the sum of squares error of the voltages on the electrodes by using one step of a regularized Newton's method. Also, various iterative methods are developed by minimizing different regularized least-squares functionals with a Tikhonov-type regularization [11][31] or a total variation regularization [3].

Solving the conductivity inverse problem with iterative algorithms requires a numerical solution of a forward problem at each iteration, therefore, the computation time accumulates fast for commonly used grid-based global methods such as the finite element method (FEM) or the boundary element method (BEM). In finding the conductivity profile to match the measured voltages over electrodes, a global solution of the potentials over the whole object is in fact not needed, therefore a global solution procedure during the forward problem incur unnecessary computational cost beyond the electrodes. With this in mind, in this paper, a local stochastic approach, a path integral Monte Carlo (PIMC) method using Feynman-Kac formula, will be proposed. Due to the nature of the Feynman-Kac formula which allows the potential solution at any single location such as those on the electrodes, we could dramatically reduce the storage and computing resources needed for each forward problem solution.

Recently, Maire and Simon [18] also proposed a probabilistic method of the voltage-to-current map using partially reflecting Brownian motions (with some given absorption and reflection probabilities on the electrodes). A walk-on-spheres (WOS) method was used to sample the paths of the Brownian motion in the interior while near the boundary, a finite difference discretization of the Laplace equation and the Robin boundary conditions were used to derive a probabilistic relation for the solution and then an integral equation with a corresponding transition probability kernel, whose solution was implemented with a Markov chain for a 2-D EIT problem [17][23]. Additionally, in [26], a random walk method based on the randomization of a boundary integral equation for the solution and a Neumann series of the involved integral operators was proposed to solve the third kind of boundary condition. In our approach, a pure probabilistic method for the voltage-to-current map uses a Feynman-Kac formula for the solution to the mixed boundary value problem, and directly simulates the reflecting Brownian motion paths as well as their local time on the boundary. It will avoid using finite difference meshing discretization, which could require a sophisticated mesh generation near the boundary of a complex and non-smooth domain, or the convergence requirement of the Neumann series of integral operators dependent on the shape of the domain. In our approach, the calculation of the boundary local time will be given careful considerations for the application of the Feynman-Kac representation. The voltages will be obtained numerically on the electrodes in a 3-D EIT problem, then the Neumann data, and henceforth the current on all electrodes.

The remainder of the paper is organized as follows. In Section 2, the forward problems of the EIT problem are introduced as well as a simplified model for the forward problem for our numerical experiments. Section 3 introduces reflecting Brownian motion (RBM), local time, and the corresponding simulation methods. Then, we propose an improved scheme for allocating the local time of the RBM and finally the path integral Monte Carlo method based on the Feynman-Kac formula for the mixed boundary value problem. In Section 4, a boundary element method (BEM) is described to generate reference solutions for validating the PIMC simulation. Comparison between the stochastic PIMC and the global BEM method, which shows the accuracy and advantages of the local and parallel PIMC method, is given in Section 5. Finally, conclusions and future work are discussed in Section 6.

2. Forward problems in EIT

In this section, we will review the forward problem arising from EIT. The mathematic models for EIT have been developed and compared with the experimental measurement of voltages on electrodes for a given conductivity distribution, which is adjusted to fit the measurements. The existing models are continuum model, gap model, shunt model, and complete electrode model. Among all, the complete electrode model was shown to be capable of predicting the experimentally measured voltages to within 0.1 percent [28] and the existence and uniqueness of the model have also been proved.

Complete electrode model [5]. The sketch map of the model is shown in Fig. 1. Let the domain of the object be denoted as Ω as shown in Fig. 1(a), embedded within which we assume there is an anomaly $\Omega_0 \subset \Omega$. The domain Ω is assumed to have a smooth boundary with a limited number of electrodes $E_l, l = 1, ..., L$ attached to $\partial\Omega$. The scalar electric potential u for the model will satisfy the following boundary value problem
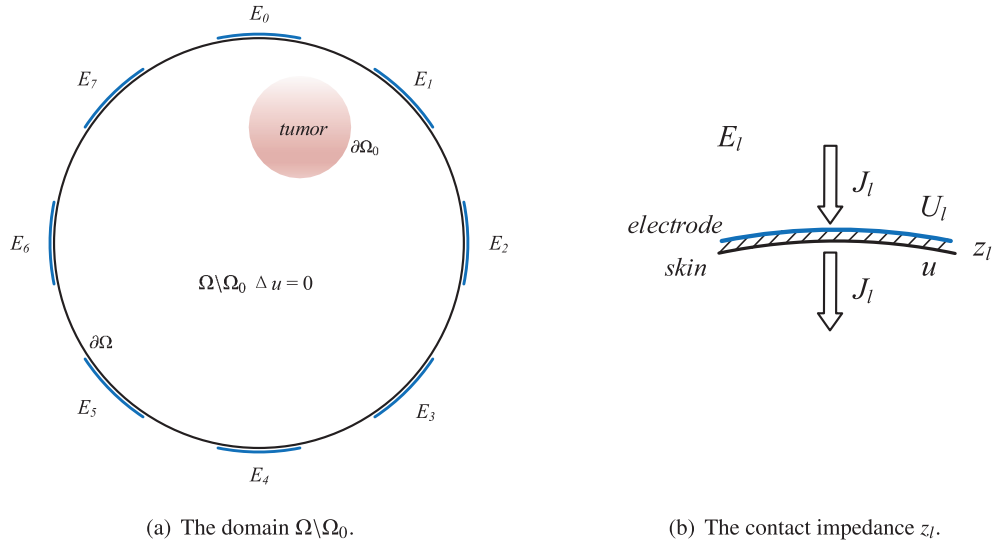
(a) The domain $\Omega\backslash\Omega_0$.

(b) The contact impedance z_l.

Fig. 1. The sketch map of the complete electrode model.

$$\nabla \cdot \gamma \nabla u = 0, \qquad \text{in } \Omega\backslash\Omega_0, \tag{1a}$$

$$\frac{1}{|E_l|} \int_{E_l} \gamma \frac{\partial u}{\partial n} dS = J_l, \qquad \text{on } E_l, \quad l = 1, 2, \cdots, L, \tag{1b}$$

$$\gamma \frac{\partial u}{\partial n} = 0, \qquad \text{on } \partial\Omega\backslash \cup_{l=1}^{L} E_l, \tag{1c}$$

$$u + z_l \gamma \frac{\partial u}{\partial n} = U_l, \qquad \text{on } E_l, \quad l = 1, 2, \cdots, L, \tag{1d}$$

$$\sum_{l=1}^{L} |E_l| J_l = 0, \tag{1e}$$

$$u = u_0 \qquad \text{on } \partial\Omega_0, \tag{1f}$$

where γ is the conductivity inside $\Omega\backslash\Omega_0$. J_l is the current density sent to the lth electrode and U_l is the corresponding measured voltage. $|E_l|$ is the area of the lth electrode and n denotes the outer unit normal vector on $\partial\Omega$.

Equation (1a) can be derived from the Maxwell equations by neglecting the time-dependence of the alternating current and assuming the current source inside the anomaly-removed portion $\Omega\backslash\Omega_0$ to be zero [28]. Equation (1b) and (1c) indicate the knowledge of current density on and off the electrodes on the boundary $\partial\Omega$, respectively. The current flows in and out through the electrodes, and no current flows through the bare skin. Equation (1d) takes account of the electrochemical effect shown in Fig. 1(b) by introducing z_l as the contact impedance or surface impedance, which quantitatively characterizes a thin, highly resistive layer at the contact between the electrode and the skin. The resistive layer limits the current densities and causes a voltage drop according to Ohm's law, and effectively reflects an important physical phenomenon occurring on the electrodes and makes the complete electrode model more realistic.

In addition, the current density J_l should satisfy equation (1e), i.e. the conservation of charge, which indicates that the sum of current on all electrodes should be zero since there is no current source inside the object. The current flowing into the object should equal that flowing out. In equation (1f), we have prescribed a constant potential u_0 on the surface of the tumor anomaly, modeled as a perfect conductor. Actually, the constant u_0 is implicitly defined through the imposed external conditions and can be determined according to equation (1e) [18].

The six equations (1a) – (1f) constitute the boundary conditions of the domain $\Omega\backslash\Omega_0$. In the inverse EIT problem, we hope to deduce the interior of the object, such as the presence or absence of the tumor and its location, through the current-voltage pairs (J_l, U_l) on the electrodes. Correspondingly, solving the forward problem is equivalent to obtaining the voltage-to-current map given a known internal configuration.

A model forward problem. In medical applications, a limited number of electrodes are attached to the human body to get surface measurements. We will illustrate our numerical method by modeling the problem inside a unit sphere. Eight electrodes are superimposed on the boundary and the centers of the electrodes all lie on the $y - z$ plane evenly, each of width 0.2. The radius of the tumor equals 0.25.

Consider the conductivity equation with boundary conditions

$$\Delta u = 0 \qquad \text{in } \Omega\backslash\Omega_0, \tag{2a}$$

$$\frac{\partial u}{\partial n} - cu = \phi_3(x) \qquad \text{on } \Gamma_3 = \cup_{l=1}^{8} E_l, \tag{2b}$$

$$\frac{\partial u}{\partial n} = \phi_2(x) \qquad \text{on } \Gamma_2 = \partial\Omega \backslash \Gamma_3, \tag{2c}$$

$$u = \phi_1(x) \qquad \text{on } \Gamma_1 = \partial\Omega_0, \tag{2d}$$

where $c = -\frac{1}{\gamma z_l}$, and γ is the conductivity, the contact impedance of the electrode z_l is a constant between 0 and 1, $\phi_3(x) = \frac{1}{\gamma z_l} U_l$, and $\phi_1(x)$ is the constant potential on the tumor, and n is the outward unit normal. For our numerical simulation, we consider specifically the case that the conductivity γ is taken to be 1, the contact impedance $z_l = 0.5$, and the imposed voltage pattern on the electrodes U_l is assigned $\cos(4\theta)$ for $x = (r, \theta, \phi)$, $\phi_2(x) = 0$.

The forward problem is a Laplace problem with mixed boundary values. The surface boundaries on or off the electrodes are given Robin or Neumann conditions while the tumor has a Dirichlet boundary. In our previous work [33][34], we described a path integral Monte Carlo simulations to find potentials given Neumann or Robin boundaries through the WOS method (described in Section 3.2). Here in this paper, a similar approach handling three kinds of boundary conditions simultaneously will be taken to find potentials on the electrode patches given mixed boundary conditions for the Laplace equation. After the potential approximations are found, the Neumann values are automatically known from the Robin boundary conditions on the electrode patches, and subsequently, the current on each electrode can be calculated according to equation (1b). Therefore, the voltage-to-current map is obtained for the forward EIT problem.

3. A path integral Monte Carlo (PIMC) solution using Feynman-Kac formula

In this section, we will first introduce reflecting Brownian motion, local time and the corresponding simulation methods, which lays the foundation of our proposed approach. Then, we will propose a more accurate allocation scheme of local time and finally the path integral Monte Carlo method based on the Feynman-Kac formula for the mixed boundary value problem in (2a)-(2d).

3.1. Reflecting Brownian motion and boundary local time

Assume that D is a domain with a C^1 boundary ∂D in R^3 and a Skorokhod problem is defined as follows:

Definition 1. Let $f \in C([0, \infty), R^3)$, a continuous function from $[0, \infty]$ to R^3. A pair $(\xi(t), L(t)) = (\xi_t, L_t)$ is a solution to the Skorokhod equation $S(f; D)$ if

1. ξ is continuous in $\bar{D}$ (the closure of D);
2. $L(t)$ is a nondecreasing function which increases only when $\xi \in \partial D$, namely,

$$L(t) = \int_0^t I_{\partial D}(\xi(s)) L(ds); \tag{3}$$

3. The Skorokhod equation holds:

$$S(f; D): \qquad \xi(t) = f(t) - \int_0^t n(\xi(s)) L(ds), \tag{4}$$

where $n(x)$ denotes the outward unit normal vector at $x \in \partial D$.

The Skorokhod problem was first studied in [27] by A.V. Skorokhod in addressing the construction of paths for diffusion processes inside domains with boundaries, which experience the instantaneous reflection at the boundaries. Skorokhod presented the result in one dimension in the form of an Ito integral and Hsu [10] later extended the concept to d-dimensions $(d \geq 2)$.

In general, the solvability of the Skorokhod problem is closely related to the smoothness of the domain D. For higher dimensions, the existence of (4) is guaranteed for C^1 domains while the uniqueness can be achieved for a C^2 domain by assuming the convexity for the domain [30]. Later, it was shown by Lions and Sznitman [16] that the constraints on D can be relaxed to some locally convex properties.

Suppose that $f(t)$ is a Brownian motion (BM) path starting at $x \in \bar{D}$ and (X_t, L_t) is the solution to the Skorokhod problem $S(f; D)$, then X_t will be the reflecting Brownian motion (RBM) on D starting at x. Because the transition probability density of the RBM satisfies the same parabolic differential equation as that for a BM, a sample path of the RBM can be simulated simply as that of the BM within the domain. However, the Neumann or Robin boundary condition for the density of RBM

implies that the path is pushed back at the boundary along the inward normal direction whenever it attempts to cross the boundary.

The boundary local time L_t is not an independent process but associated with RBM X_t and defined by

$$L(t) \equiv \lim_{\epsilon \to 0} \frac{\int_0^t I_{D_\epsilon}(X_s)ds}{2\epsilon}, \tag{5}$$

where D_ϵ is a strip region of width ϵ containing ∂D and $D_\epsilon \subset \overline{D}$. Here L_t is the local time of X_t, a notion invented by P. Lévy [14]. This limit exists both in L^2 and P^x-a.s. for any $x \in \overline{D}$.

It is obvious that L_t measures the amount of time that the reflecting Brownian motion X_t spends in a vanishing neighborhood of the boundary within the time period $[0, t]$. An interesting part of (5) is that the set $\{t \in R_+ : X_t \in \partial D\}$ has a zero Lebesgue measure while the sojourn time of the set is nontrivial [12]. This concept is not just a mathematical one but also has physical relevance in understanding the "crossover exponent" associated with "renewal rate" in modern renewal theory [7].

3.2. Simulation of RBM and the corresponding local time

The walk-on-spheres (WOS) method was first proposed by Müller [20], which can solve the Dirichlet problem for the Laplace operator efficiently.

To illustrate the WOS method for the Dirichlet problem of Laplace equation, with Dirichlet boundary conditions ϕ_1, the solution can be rewritten in terms of a measure μ_D^x defined on the boundary ∂D,

$$u(x) = E^x(\phi_1(X_{\tau_D})) = \int_{\partial D} \phi_1(y)d\mu_D^x, \tag{6}$$

where τ_D is the first time a Brownian path hits the Dirichlet boundary ∂D and μ_D^x measures the probability of the Brownian paths originating from the point x in D and hitting a given boundary area,

$$\mu_D^x(F) = P^x\{X_{\tau_D} \in F, X_0 = x\}, F \subset \partial D, x \in D. \tag{7}$$

The harmonic measure μ_D^x can be shown to be related to the Laplacian Green's function $g(x, y)$ in the domain D with a homogeneous boundary condition [6], i.e.,

$$-\Delta g(x, y) = \delta(x - y), \quad x, y \in D,$$

$$g(x, y)|x \in \partial D = 0.$$

By comparing (6) with the following integral representation of the solution of the Laplace equation using Green's second identity in terms of the Green's function $g(x, y)$,

$$u(x) = -\int_{\partial D} \phi_1(y) \frac{\partial g(x, y)}{\partial n_y} ds_y, \tag{8}$$

we can see that the hitting probability, now denoted as $p(x, y)ds_y = \mu_D^x([y, y + ds_y])$, has the following connection to the Green's function of the domain D [32],

$$p(x, y) = -\frac{\partial g(x, y)}{\partial n_y}. \tag{9}$$

Therefore, if the starting point x of Brownian motion is at the center of a spherical domain, the probability of the BM path hitting the boundary of the sphere will be uniform. This fact is the basis for the WOS method, which allows us to simulate the Brownian motion using a sequence of walks or jumps over spheres. To be specific, given a starting point x inside the domain D, we can draw a sphere centered at x which does not intersect with the domain boundary ∂D and sample the next location of the Brownian path on the surface of the sphere using a uniform distribution, say at x_1. Then, treat x_1 as the new starting point, draw a second sphere fully contained in D, make a jump from x_1 to x_2 on the surface of the second sphere as before. The jumps of the particle in the WOS method are illustrated in Fig. 2(a). Repeat this procedure until the path hits an absorption ϵ-shell of the domain [8]. When this happens, we assume that the path has hit the boundary ∂D and terminated. The location of the hitting point is denoted as X_{τ_D} and the corresponding value of the boundary data $\phi_1(X_{\tau_D})$ is recorded.

Now we can define an estimator of (6) by

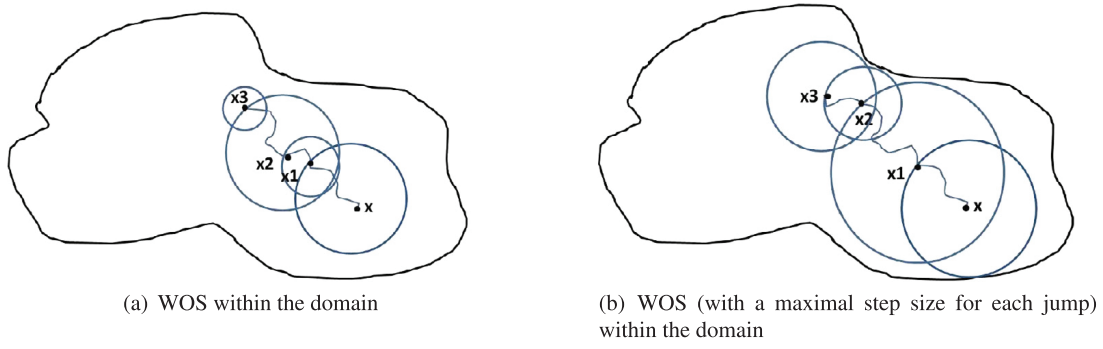$$u(x) \approx \frac{1}{N} \sum_{i=1}^{N} \phi_1(x_i), \tag{10}$$

(a) WOS within the domain

(b) WOS (with a maximal step size for each jump) within the domain

Fig. 2. Walk-on-spheres method.

(a) A ϵ-region for a bounded domain in R^3
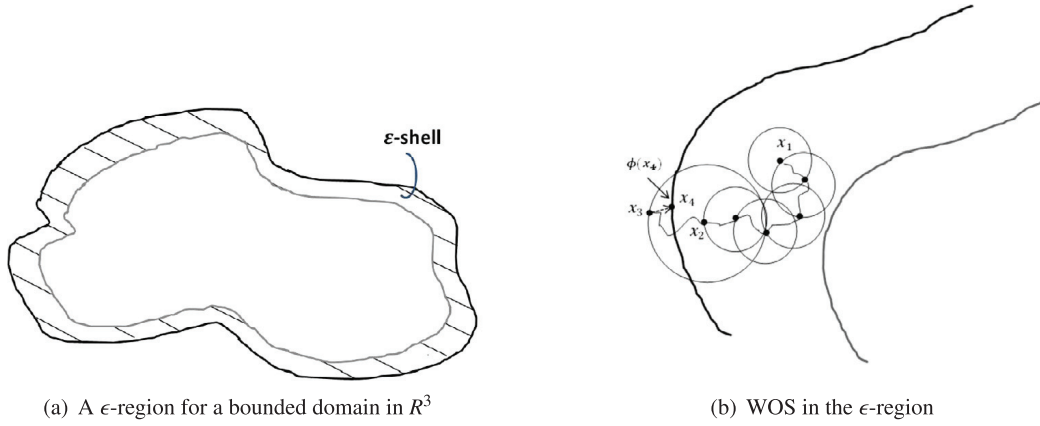
(b) WOS in the ϵ-region

Fig. 3. Walk on Spheres near the boundary.

where N is the number of Brownian paths sampled and x_i is the first hitting point of each path on the boundary. To speed up the WOS process, the maximum possible size of the sphere for each step can be adopted to allow faster first hitting on the boundary as shown in Fig. 2(b). Specifically, the radius of each sphere is set to the distance from this point to the domain boundary.

The simulation of the RBM path is the same as the BM path except the reflection on the reflecting (Neumann or Robin) boundary. For the reflecting boundary, we will construct a strip region with width ϵ around the boundary (see Fig. 3(a)) and allow the process X_t to move according to the law of BM continuously. Before the path enters the $\epsilon-$ region, the radius of WOS is chosen to be of a maximum possible size with the distance to the boundary. Once the particle is in the strip region, the radius of the WOS sphere is then fixed at a constant Δx (or $2\Delta x$, see Fig. 3(b)). If the path attempts to pass crosses the reflecting boundary, the path will be pull back to the nearest point on the boundary and continue the random walk. With this simulation for the reflection, according to the definition (5), the corresponding local time may be interpreted as
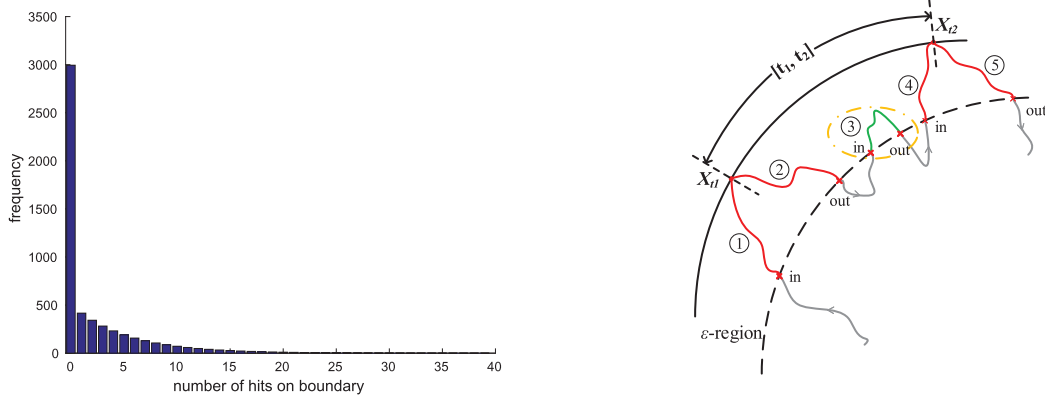
$$L(t) \approx \frac{\int_0^t I_{D_\epsilon}(X_s)ds}{2\epsilon}. \tag{11}$$

It is known that the elapsed time $\triangle t$ for a step of a random walk on average is proportional to the square of the step size, in fact, $\triangle t = (\triangle x)^2/d, d = 3$ when $\triangle x$ is small, which can also be applied to WOS moves. The relevant proof is referred to the appendix of [34]. Thus, the increment of local time during the time interval $[t, t+dt]$ can be obtained by accumulating the amount of each step inside the ϵ-region, i.e.

$$dL(t) = L(t+dt) - L(t) \approx \frac{\int_t^{t+dt} I_{D_\epsilon}(X_s)ds}{2\epsilon} \approx (n_{t+dt} - n_t)\frac{(\Delta x)^2}{6\epsilon}, \tag{12}$$

given a prefixed radius Δx inside the ϵ-strip region and n_t is the cumulative steps that path stays within the ϵ-region from the beginning until time t (see **Remark I** for definition). Notice that only those steps where the path of X_t stays in the ϵ-region will contribute to n_t while the RBM may stay out of the ϵ-region at other steps. More details can be found in [34].

Remark I. Occupation time of RBM X_t in the numerator of (11) was calculated in terms of that of BM sampled by the walks on spheres. Notice here that within the ϵ-region, the radius of the WOS may be Δx or $2\Delta x$, which implies that the corresponding elapsed time of one step for local time could be $(\Delta x)^2/3$ or $(2\Delta x)^2/3$. The latter is four times bigger than the former. But if we absorb the factor 4 into n_t, (12) will still hold. In practical implementation, we treat n_t as a vector of

(a) The occurrence frequency of different numbers of hits on boundary between an entry into and an exit out of the ϵ-region. Numerical parameters: Spherical domain with a Neumann data, $NP = 8e4, \Delta x = 5e - 4, \epsilon = 2.5\Delta x$. 56.06% of cases found with no collision on the boundary.

(b) A schematic diagram of typical scenery of a path hitting the reflecting boundary.

Fig. 4. The scenery of the path hitting the reflecting boundary.

entries of increasing value, the increment of each component of n_t over the previous one after each step of WOS will be 0, 1 or 4, corresponding to the scenarios that X_t is out of the ϵ-region, in the ϵ-region while sampled on the sphere of a radius Δx, or in the ϵ-region while sampled on the sphere of a radius $2\Delta x$, respectively. The increase of the radius from Δx to $2\Delta x$ is to sample the collision of the path of the boundary more efficiently.

3.3. A more accurate allocation scheme of local time

A new allocation scheme of local time with a better accuracy will be proposed, which is of great significance in the calculation of numerical solution based on the Feynman-Kac formula for Neumann or Robin boundary conditions. Taking a Neumann problem as an example, we consider a domain D with a Neumann boundary condition ϕ_2. The Feynman-Kac formula provides a local solution for the potential u inside the domain D through stochastic processes as follows [10],

$$u(x) = E^x \left\{ \int_0^\infty \phi_2(X_t) dL(t) \right\}, \tag{13}$$

where X_t is the reflecting Brownian motion, $L(t)$ is the corresponding local time. It is noted that the integral for the Neumann data $\phi_2(X_t)$ differs from the formula in [10] without the factor of 1/2 due to a different definition of the local time here (as also reflected in the Skorokhod equation).

The numerical approximation will be then given by

$$\tilde{u}(x) = E^x \left\{ \sum_{j'=0}^{NP} \phi_2(X_{t_j}) dL(t_j) \right\}, \tag{14}$$

where the expectation E^x is taken as the average of all RBM paths starting from x, NP is the length of the sample paths, j' denotes each step of the path and j denotes the steps where the path hits a reflecting boundary, i.e. Neumann boundary in this case. The simulations of the RBM paths will follow the description in Section 3.2. Whenever a RBM path collides with the reflecting boundary, say at X_{t_j}, the corresponding boundary condition $\phi_2(X_{t_j})$ is recorded, and the corresponding local time increment $dL(t_j)$ should be an important weight in the path integral.

In our previous work [33] and [34], the local time increment $dL(t_j)$ is simply approximated by

$$dL(t_j) \approx (n_{t_j} - n_{t_{j-1}}) \frac{(\Delta x)^2}{6\epsilon}, \tag{15}$$

where t_{j-1} and t_j are two consecutive collisions that a path has with the reflecting boundary and $n_{t_j} - n_{t_{j-1}}$ will be the increment of the vector of the local time defined in **Remark I** between these two collisions.

However, we will illustrate that this allocation of local time is not completely appropriate and a new scheme is thus proposed here. On a closer examination of the path collision history inside the ϵ-region, there are many cases where paths enter the ϵ-region and come out without colliding with the boundary as in Fig. 4(a), the frequency of which is even more than 50%. According to the approximate formula (11), these cases generate local time. However, this is actually an error
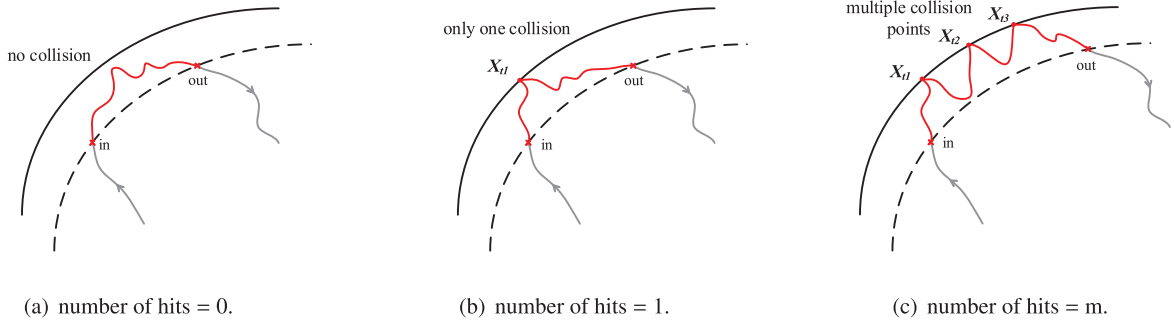
(a) number of hits = 0.   (b) number of hits = 1.   (c) number of hits = m.

Fig. 5. Three situations of the path walking in the ϵ-region.

caused by the approximation, namely the width of the ϵ-region. According to strict definition of local time (3), these cases should not generate local time because the path does not hit the boundary during the time intervals.

Fig. 4(b) is a schematic diagram depicting the situation where the path collides with the boundary twice and is reflected. Part ② represents the segment from the previous collision point to the exit out of ϵ-region, Part ③ represents the segment where the path enters the ϵ-region and comes out without colliding with the boundary, and Part ④ represents the segment from the re-entry to the next collision point. In the calculation method in (15), Part ②, Part ③ and Part ④ are considered as the local time increment corresponding to collision point X_{t_2}, which counts mistakenly the increment caused by the path entering the ϵ-region but not hitting the boundary between the two collision points (Part ③). Meanwhile, Part ② is far from collision point X_{t_2}, and it is inappropriate to count it as the corresponding local time increment of X_{t_2} and further as the weight for $\phi_2(X_{t_2})$.

To redress the error caused during the allocation scheme of local time increment, we propose a new allocation scheme of local time instead. We keep track of each entry (t_{in}) and exit time (t_{out}) of the path into the ϵ-region, and then allocate the local time increment for each possible collision within this time period. Namely, to compute more accurate δn_{t_j} corresponding to the collision point X_{t_j}, we record the increment of the vector of the WOS steps $n_{j,out} - n_{j,in}$ between one entry into and one exit out of the ϵ-region by a path during this period X_{t_j} takes, and also the number of collisions m_j at the boundary during the same time period, and then set

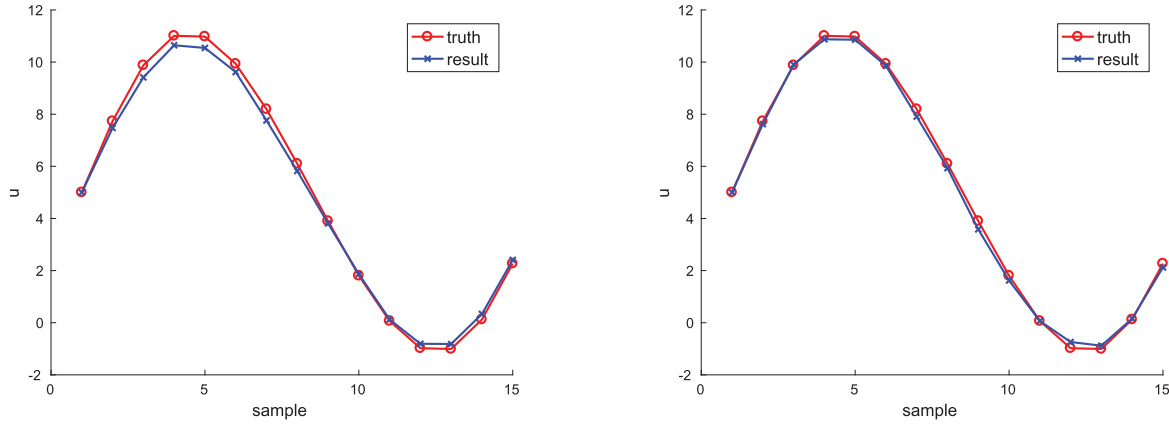$$dL(t_j) = \delta n_{t_j} \frac{(\Delta x)^2}{6\epsilon}, \tag{16}$$

where

$$\delta n_{t_j} = \begin{cases} \frac{n_{j,out} - n_{j,in}}{m_j}, & \text{if } m_j > 0 \\ 0, & \text{if } m_j = 0 \end{cases}, \tag{17}$$

which should give $\delta n_{t_j} = 0$ in Fig. 5(a), $\delta n_{t_j} = n_{j,out} - n_{j,in}$ in Fig. 5(b), and $\delta n_{t_j} = \frac{n_{j,out} - n_{j,in}}{m_j}$ for each collision in Fig. 5(c). Considering that the RBM path may be truncated by the length NP, in the last special case, when the path is truncated within the ϵ-region, the truncation will be regarded as an exit, that is $t_{out} = t_{NP}$.

The new approach in allocating the local time has greatly improved the accuracy of the numerical solution. Compared with about 4% error achieved by the previous method, the new approach can reduce the error to 1%. Here, we give one example of the Neumann problem to illustrate the improvement in a test case in [34]. The numerical results calculated by two different ways of allocating the local time increment at each collision on boundary are shown in Fig. 6. Using the new allocation method for the local time, numerical experiments show that the result is optimal when the jump distance in the reflecting boundary region Δx is set to be 5e-4 and the width of the ϵ-region $\epsilon = 1.4\Delta x$. These two values are used in all of our numerical experiments, including the Neumann problem, the Robin problem and the mixed boundary value problem, and all the experiments achieve good results. When the number of Monte Carlo simulations N is large enough, as the path length parameter NP increase, the simulation result converges to the true reference value with an error of 1%. We also note that with the previous computational method for the local time, the optimal choice for the width of the ϵ-region was found also by numerical experiments to be $\epsilon = 2.5\Delta x$.

Remark II. We emphasize that in the process of simulating the RBM, three situations should be considered, which are shown in Fig. 5(a)-5(c). When the path travels in the ϵ-region but does not collide with the boundary as indicated in Fig. 5(a), we declare that there is no local time generated subject to strict definition (3), and no contribution to the path integral. When the path hits the reflecting boundary once during walking in the ϵ-region, the local time increment corresponding to the collision point equals the local time generated by the path walking in the ϵ-region. In all other cases where the path collides with the boundary multiple times after entering the area as shown in Fig. 5(c), the generated local time increment is evenly distributed to these several collision points.

(a) The original method; $N = 2e5$, $NP = 3e4$, $\Delta x = 5e - 4$, $\epsilon =$ 2.5Δx; average error = 3.96% (5.13% reported in the original text).

(b) The modified method; $N = 2e5$, $NP = 3e4$, $\Delta x = 5e - 4$, $\epsilon = 1.4\Delta x$; average error = 1.38%.

Fig. 6. The PIMC results for potential on 15 points inside a sphere for a Neumann problem of the Laplace equation with an exact solution $u = \sin 3x \sin 4y e^{5z} + 5$, calculated by two different ways of local time: (left) local time by (15), (right) local time by (16).

3.4. PIMC based on Feynamn-Kac formula for the mixed boundary value problem

We consider the mixed boundary value problem in the domain $\Omega \backslash \Omega_0$ satisfying equation (2a)-(2d). A probabilistic solution for the mixed boundary value problem is given by a Feynman-Kac formula [19][22] (the factor $\hat{e}_c$ was left out inadvertently in the formula on the Dirichlet and Neumann boundary part in [22])

$$u_{Mix}(x) = E^x \left\{ \int_0^{\tau_{\Gamma_1}} \hat{e}_c(t)\phi_{2,3}(X_t)dL(t) \right\} + E^x(\hat{e}_c(\tau_{\Gamma_1})\phi_1(X_{\tau_{\Gamma_1}})). \tag{18}$$

where the expectation E^x is taken as the average of all paths starting from x, $\phi_{2,3}$ means the given Neumann or Robin boundary conditions, i.e. ϕ_2 or ϕ_3. X_t is the reflecting Brownian motion, $L(t)$ is the corresponding local time, τ_{Γ_1} is the first time a Brownian path hits the Dirichlet boundary $\partial\Omega_0 = \Gamma_1$, and the definition of the Feynman-Kac functional $\hat{e}_c(t)$ is

$$\hat{e}_c(t) := e^{\int_0^t c(X_s)dL(s)}. \tag{19}$$

The introduction of the Feynman-Kac functional $\hat{e}_c(t)$ is important for the Robin boundary and accurately reflects the influence of the Robin boundary conditions in the probabilistic solution. For the mixed boundary problem just with the Dirichlet and Neumann boundary, the functional (19) equals 1. However, once the Robin boundary is involved, the functional will not be 1 and be applied over the entire sampling path as an attenuation coefficient. Thus, the functional should influence all of the integral terms, not just the one related to the Robin boundary conditions.

It is noted that although the form of the integral terms corresponding to the Neumann and Robin boundary conditions is the same, there is an implicit difference due to the definition of the functional (19). Because the functional (19) is only related to the given parameter $c(X_s)$ on the Robin boundary, its value changes only when the path hits the Robin boundary. Every time the path hits the Robin boundary, there is a sudden decrease in the value of the functional. With the increase of the reflections by the Robin boundary, the functional changes from 1 to 0 gradually, leading to attenuation of subsequent integral term contributions and the final convergence of the path integral. When $t = \tau_{\Gamma_1}$, the Brownian path hits the Dirichlet boundary and is absorbed, and $\hat{e}_c(\tau_{\Gamma_1})$ denotes the final attenuation at this time.

When the time interval is truncated to $[0, T]$ or identified with the length of sample path NP, the numerical approximation to (18) will be

$$\tilde{u}_{Mix}(x) = E^x \left\{ \int_0^T \hat{e}_c(t)\phi_{2,3}(X_t)dL(t) \right\} + E^x(\hat{e}_c(\tau_{\Gamma_1})\phi_1(X_{\tau_{\Gamma_1}})), \tag{20}$$

or

$$\tilde{u}_{Mix}(x) = E^x \left\{ \sum_{j'=0}^{NP} \hat{e}_c(t_j)\phi_{2,3}(X_{t_j})dL(t_j) \right\} + E^x(\hat{e}_c(\tau_{\Gamma_1})\phi_1(X_{\tau_{\Gamma_1}})). \tag{21}$$

Equivalently,

$$\tilde{u}_{Mix}(x) = E^x \left\{ \sum_{j:X_{t_j} \in \Gamma_2 \cup \Gamma_3}^{NP} \hat{e}_c(t_j)\phi_{2,3}(X_{t_j})dL(t_j) \right\} + E^x(\hat{e}_c(\tau_{\Gamma_1})\phi_1(X_{\tau_{\Gamma_1}})), \tag{22}$$

where j' denotes each step of the path, j denotes the steps where the path hits the reflecting boundary. The approximation of Feynman-Kac functional $\hat{e}_c(t)$ is

$$\hat{e}_c(t) \approx e^{\sum_{t_k \leq t} c(X_{t_k})dL(t_k)}, \quad t = t_j \text{ or } \tau_{\Gamma_1}, \tag{23}$$

where $t_k : X_{t_k} \in \Gamma_3$, i.e. k denotes the steps where the path hits the Robin boundary before the time t. Similar to what we stated earlier in the Neumann problem, the local time increment $dL(t_k)$ allocated for each collision X_{t_k} should be a weight for the corresponding parameter $c(X_{t_k})$ in the integral of the functional $\hat{e}_c(t)$.

Therefore, everytime a RBM path collides with the reflecting boundary, say at X_{t_j}, the corresponding boundary condition $\phi_{2,3}(X_{t_j})$ is recorded, the corresponding local time increment $dL(t_j)$ and the current value of the functional $\hat{e}_c(t_j)$ are the weights, and thus the value of the term $\delta u(X_{t_j}) = \hat{e}_c(t_j)\phi_{2,3}(X_{t_j})dL(t_j)$ at the collision point X_{t_j} is counted in the cumulative sum for the path integral. If the RBM path is absorbed by the Dirichlet boundary Γ_1 before the truncation, the value of the term $\delta u(X_{\tau_{\Gamma_1}}) = \hat{e}_c(\tau_{\Gamma_1})\phi_1(X_{\tau_{\Gamma_1}})$ is counted in the cumulative sum as the last term.

Adopting our proposed new allocation scheme of the local time defined in (16), we have

$$\hat{e}_c(t_j) = e^{\sum_{k=0}^{j} c(X_{t_k})\delta n_{t_k} \frac{(\Delta x)^2}{6\epsilon}}, \tag{24}$$

$$\hat{e}_c(\tau_{\Gamma_1}) = e^{\sum_{t_k < \tau_{\Gamma_1}} c(X_{t_k})\delta n_{t_k} \frac{(\Delta x)^2}{6\epsilon}}. \tag{25}$$

So, finally, we have the approximation to the probabilistic solution (18)

$$\tilde{u}_{Mix}(x) = E^x \left\{ \sum_{j'=0}^{NP} e^{\sum_{k=0}^{j} c(X_{t_k})\delta n_{t_k} \frac{(\Delta x)^2}{6\epsilon}} \phi_{2,3}(X_{t_j})\delta n_{t_j} \frac{(\Delta x)^2}{6\epsilon} \right\} + E^x(e^{\sum_{t_k < \tau_{\Gamma_1}} c(X_{t_k})\delta n_{t_k} \frac{(\Delta x)^2}{6\epsilon}} \phi_1(X_{\tau_{\Gamma_1}})). \tag{26}$$

3.5. Algorithm details for the PIMC method for mixed boundary problems

Using the simulation of RBM and the modified statistical method, Algorithm 1 gives a pseudo-code for the numerical realization of the proposed path integral Monte Carlo method for mixed boundary problems.

For RBM in a domain given mixed boundary conditions, the random walk path is reflected on the Neumann or Robin boundary and is absorbed on the Dirichlet boundary. Specifically in the forward EIT problem, it is necessary to consider the distances to sphere and tumor, respectively. When the path enters the respective strip region of the absorbing or reflecting boundary, the corresponding operation needs to be completed, that is, the path is reflected on $\partial\Omega$ or absorbed on $\partial\Omega_0$.

In the Algorithm 1, code in line 4 - line 14 illustrates the transition from the current point to a new point according to the current position. If the point is in the strip region around the reflecting boundary, the radius of the jump will be changed to Δx or $2\Delta x$ and corresponding local time increment will be recorded (line 7 - line 12). When the next point is outside the reflecting boundary, a forced drawing back operation needs to be done (line 15 - line 18). Once the point hits the boundary, the value and the type of boundary need to be recorded for the follow-up data processing (line 19 - line 27). If the number of transition counts up to NP and the path has not been absorbed, the path will be truncated compulsively. The path integral is calculated with formula (26) after each path ends.

In order to obtain accurate mathematical expectations, a large number of paths should be sampled and the potential approximation of the starting point is calculated as the average of these path integrals.

4. A deterministic solution with the boundary element method

To provide reference solutions to the path integral MC method proposed above, we will present a deterministic method based on boundary element method for the mixed boundary value problem (2a)-(2d).

4.1. Graded boundary mesh

For boundary element method for the simplified forward model, a specially designed boundary mesh must be established over electrodes. Boundary mesh on $\partial\Omega$ is constructed on the electrode patches and off-electrodes, respectively, as shown in Fig. 7. For our implementation, GMSH is used to generate an unstructured 2D mesh consisting of flat triangles given the size of each triangle on off-electrode patch, and a simple mapping will fit the grid to the boundary. On the electrode patches, the meshes are structured in such a way that mesh points are located at the intersection of divisions along the longitude

---

Algorithm 1 PIMC method for mixed boundary problems.

Input: The information of the domain and the boundary, the number of Monte Carlo simulations N, the length of each path NP, the starting point X_0, the width of the ϵ-region of the reflecting boundary $\epsilon_{reflecting}$, the step size of the WOS inside the ϵ-region near the reflecting boundary Δx, and the width of the absorption ϵ-shell of the absorbing boundary $\epsilon_{absorbing}$.
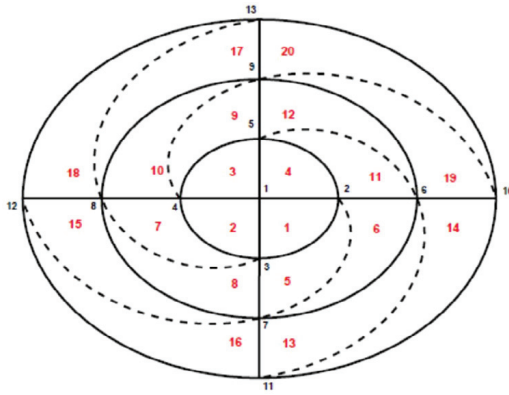
Output: An approximation of $u(X_0)$.

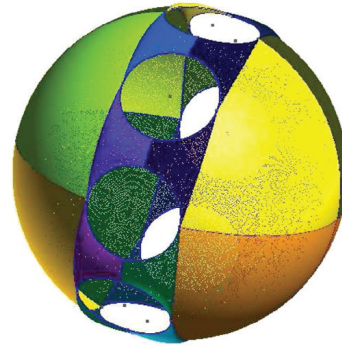**Initialization:** local time $L[NP]$, boundary value $v[NP]$ and boundary type $type[NP]$.

1: **for** $pathcount = 1 : N$ **do**
2:      $X = X_0$
3:      **for** $stepcount = 1 : NP$ **do**
4:          $R_r =$ the distance from X to the reflecting boundary;
5:          $R_a =$ the distance from X to the absorbing boundary;
6:          $R_{max} = min\{R_r, R_a\}$;
7:          **if** $0 < R_r \le \Delta x$ **then**
8:              $R_{max} = 2\Delta x$, $L[stepcount] = 4$;
9:          **end if**
10:         **if** $\Delta x < R_r < \epsilon_{reflecting}$ or $R_r = 0$ **then**
11:             $R_{max} = \Delta x$, $L[stepcount] = 1$;
12:         **end if**
13:         Make a sphere with the current point as the center and R_{max} as the radius;
14:         Take a new point X_t on the sphere with uniform probability;
15:         **if** X_t is outside the reflecting boundary **then**
16:             Find a point X_c on the reflecting boundary which is closest to X_t;
17:             $X_t = X_c$;
18:         **end if**
19:         **if** X_t is on the reflecting boundary **then**
20:             $v[stepcount] = \varphi(X_c)$;
21:             $type[stepcount]$ records type of boundary(Neumann: 2, Robin: 3);
22:         **end if**
23:         $R_a =$ the distance from X_t to the absorbing boundary;
24:         **if** $R_a \le \epsilon_{absorbing}$ **then**
25:             $v[stepcount] = \varphi(X_t)$;
26:             $type[stepcount] = 1$;
27:             End the walk path;
28:         **else** $X = X_t$;
29:         **end if**
30:     **end for**
31:     Calculate the path integral with L, v and $type$ using formula (26).
32: **end for**
33: **return** $u(X_0)$ = the average of the integrals of all paths.

(a) Curved triangular mesh on an electrode   (b) Curved triangular mesh off-electrode patches

Fig. 7. Curved triangular meshes for EIT problem.

and altitude to give a body-fitted mesh and the mapping from the elemental triangle to the curved ones can be found in [15]. On the surface of the tumor $\partial \Omega_0$, meshes are structured in a similar way by divisions along the latitude and longitude of $\partial \Omega_0$. A global boundary integral equation can then be set up with the meshes on $\partial \Omega$ and $\partial \Omega_0$.

A close look at the boundary conditions in (2b) and (2c) reveals discontinuities in potential at the rims of all the electrodes. Therefore, it is natural to enlarge the meshing area for the electrode E_i so that we have more control over the mesh size for better accuracy. Assume the enlarged radius to be $r_e = 0.3$. Because of the discontinuities, we consider a graded mesh on the enlarged surface by introducing a layered mesh structure, as Fig. 8 illustrates. There are four layers: the first ranges from center to r_1, second from r_1 to r, third from r to r_2 and fourth from r_2 to r_e. A dense mesh will be used
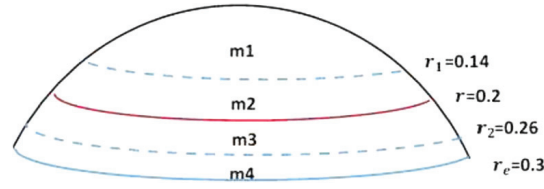
Fig. 8. Graded mesh on electrode patches.

around the rim ($r = 0.2$) of the electrode, namely, both the 2nd layer and 3rd layer should have a decreasing mesh size towards $r = 0.2$. Furthermore, a graded mesh also discretizes the first layer while an evenly distributed mesh is used on the fourth layer. And m_1, m_2, m_3 and m_4 are the number of divisions along the altitude in each layer, respectively. Here we take $m_1 = 15, m_2 = 12, m_3 = 12$ and $m_4 = 7$. The mesh size can be calculated through $dx \cdot \alpha^i, i = 0, ..., m_j - 1 (\alpha = 3/4, j = 1, 2, 3, 4)$. The number of divisions along the longitude is the same for each layer, i.e. $n = 60$. There are 55300 mesh points and 109588 flat triangle elements on off-electrode patch as shown in Fig. 7(b) and the numbers of divisions along the latitude and longitude of Ω_0 are 50 and 60, respectively.

4.2. Boundary integral equation

By using Green's second identity, we have the following relation for any fixed $x \in \Omega \backslash \Omega_0$,

$$\int_{\Omega \backslash \Omega_0} (u(y)\Delta G(x, y) - G(x, y)\Delta u(y)) \, dy = \int_\Gamma \left(\frac{\partial G(x, y)}{\partial n_y} u(y) - G(x, y)\frac{\partial u(y)}{\partial n_y} \right) ds_y, \tag{27}$$

where $\Gamma = \partial\Omega \bigcup \partial\Omega_0 = \Gamma_1 \cup \Gamma_2 \cup \Gamma_3$ and $G(x, y)$ is the fundamental solution of the Laplace operator, namely,

$$G(x, y) = \frac{1}{4\pi} \frac{1}{|x - y|}. \tag{28}$$

As $x \to \Gamma$ from $\Omega \backslash \Omega_0$, we obtain for $x \in \Gamma$,

$$\frac{1}{2}u(x) = \int_\Gamma G(x, y)\frac{\partial u(y)}{\partial n_y} ds_y - \int_\Gamma \frac{\partial G(x, y)}{\partial n_y} u(y) ds_y,$$

$$= \int_{\partial\Omega \bigcup \partial\Omega_0} G(x, y)\frac{\partial u(y)}{\partial n_y} ds_y - \int_{\partial\Omega \bigcup \partial\Omega_0} \frac{\partial G(x, y)}{\partial n_y} u(y) ds_y \tag{29}$$

If we substitute the boundary conditions on the three kinds of boundaries (2b)-(2d) into the equation, when $x \in \Gamma_2 \cup \Gamma_3$, i.e. $\partial\Omega$, the equation becomes

$$\frac{1}{2}u(x) = \int_{\Gamma_3} G(x, y)(\phi_3(y) + cu(y)) ds_y - \int_{\Gamma_3} \frac{\partial G(x, y)}{\partial n_y} u(y) ds_y + \int_{\Gamma_2} G(x, y)\phi_2(y) ds_y \tag{30a}$$

$$- \int_{\Gamma_2} \frac{\partial G(x, y)}{\partial n_y} u(y) ds_y + \int_{\Gamma_1} G(x, y)\frac{\partial u(y)}{\partial n_y} ds_y - \int_{\Gamma_1} \frac{\partial G(x, y)}{\partial n_y} \phi_1(y) ds_y,$$

or when $x \in \Gamma_1$, i.e. $\partial\Omega_0$, the equation becomes

$$\frac{\phi_1(x)}{2} = \int_{\Gamma_3} G(x, y)(\phi_3(y) + cu(y)) ds_y - \int_{\Gamma_3} \frac{\partial G(x, y)}{\partial n_y} u(y) ds_y + \int_{\Gamma_2} G(x, y)\phi_2(y) ds_y \tag{30b}$$

$$- \int_{\Gamma_2} \frac{\partial G(x, y)}{\partial n_y} u(y) ds_y + \int_{\Gamma_1} G(x, y)\frac{\partial u(y)}{\partial n_y} ds_y - \int_{\Gamma_1} \frac{\partial G(x, y)}{\partial n_y} \phi_1(y) ds_y.$$

After taking $u(x)$ on $\partial\Omega$ and $\frac{\partial u(x)}{\partial n_x}$ on $\partial\Omega_0$ as the unknowns, substituting the parameters and rearranging the equation, we obtain a global boundary integral equation for the forward EIT problem

$$\frac{1}{2}u(x) + \int_{\Gamma_3} \left(\frac{\partial G(x, y)}{\partial n_y} - G(x, y)c\right)u(y) ds_y + \int_{\Gamma_2} \frac{\partial G(x, y)}{\partial n_y} u(y) ds_y - \int_{\Gamma_1} G(x, y)\frac{\partial u(y)}{\partial n_y} ds_y$$

Table 1
The influence of the tumor position on electrode potential.

tumor			potential at $(0,0,1)$		
position	radius	potential	no tumor	with tumor	difference
$(0.5, 0, 0)$		-0.01957		0.233339	0.121%
$(0, 0, 0)$		-0.01962		0.233342	0.122%
$(0, 0, 0.25)$		-0.01940		0.232866	-0.082%
$(0, 0, 0.4)$		-0.01700		0.230048	-1.292%
$(0, 0, 0.5)$	0.25	-0.01225	0.233058	0.223350	-4.165%
$(0, 0, 0.6)$		-0.00222		0.202139	-13.267%
$(0, 0, 0.7)$		0.01806		0.120227	-48.413%
$(0.169, 0.197, 0.541)$		-0.01850		0.223928	-3.917%
$(0.183, 0.213, 0.586)$		-0.01775		0.220476	-5.399%

$$= \int_{\Gamma_3} G(x, y)\phi_3(y)ds_y - u_0 \int_{\Gamma_1} \frac{\partial G(x, y)}{\partial n_y}ds_y, \quad x \in \partial\Omega \tag{31a}$$

$$\int_{\Gamma_3} (\frac{\partial G(x, y)}{\partial n_y} - G(x, y)c)u(y)ds_y + \int_{\Gamma_2} \frac{\partial G(x, y)}{\partial n_y}u(y)ds_y - \int_{\Gamma_1} G(x, y)\frac{\partial u(y)}{\partial n_y}ds_y$$

$$= \int_{\Gamma_3} G(x, y)\phi_3(y)ds_y - (\frac{1}{2} + \int_{\Gamma_1} \frac{\partial G(x, y)}{\partial n_y}ds_y)u_0, \quad x \in \partial\Omega_0. \tag{31b}$$

Equation (31a) is the equation for $x \in \partial\Omega$ and (31b) is the equation for $x \in \partial\Omega_0$. With the different meshes on $\partial\Omega$ and $\partial\Omega_0$, letting x loop over all the mesh points, we have a linear system for solving $u(x)$ on $\partial\Omega$ and $\frac{\partial u(x)}{\partial n_x}$ on $\partial\Omega_0$ and the equation dimension equals the number of the mesh points on $\partial\Omega \bigcup \partial\Omega_0$. The potential inside the domain can be computed through

$$u(x) = \int_\Gamma G(x, y)\frac{\partial u(y)}{\partial n_y}ds_y - \int_\Gamma \frac{\partial G(x, y)}{\partial n_y}u(y)ds_y, \tag{32}$$

where $\frac{\partial u(y)}{\partial n_y}$, the Neumann values on Γ_3, are automatically known once the reference potentials are found on the electrode patches from the Robin conditions (2b).

For comparison, we also need to calculate the solution of the case without the tumor Ω_0. The spherical domain is empty and $\Gamma = \partial\Omega = \Gamma_2 \cup \Gamma_3$. The boundary integral equation is built for mesh points on $\partial\Omega$ and the derivation is similar to the process above. The adjusted equation below can be obtained.

$$\frac{1}{2}u(x) + \int_{\Gamma_3} (\frac{\partial G(x, y)}{\partial n_y} - G(x, y)c)u(y)ds_y + \int_{\Gamma_2} \frac{\partial G(x, y)}{\partial n_y}u(y)ds_y = \int_{\Gamma_3} G(x, y)\phi_3(y)ds_y, \quad x \in \partial\Omega. \tag{33}$$

The equation dimension equals the number of all the mesh points on $\partial\Omega$. From the equation, we can work out $u(x)$ on $\partial\Omega$ and obtain the global potential distribution though (32), again.
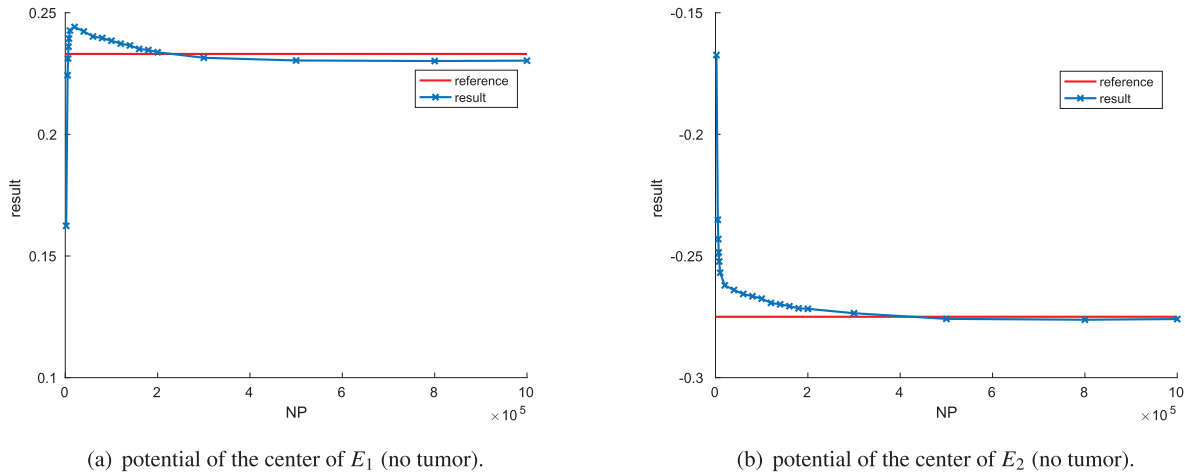
4.3. Tumor locations and electrode potential and current computed by BEM

In order to confirm the numerical results of proposed PIMC method, the BEM discussed above will be used to produce a reference solution for the forward EIT problem. As the effect of the tumor on the electrodes depends on the location of the tumor, we exam first the potential at the center of the north pole electrode (0,0,1) for our study. The result in Table 1 shows that the tumor has a bigger effect on the closest electrode. If the distance is large, the difference between the case with and without the tumor may be too small to be distinguished in experiments.

In the following numerical experiments, we will set the position of the tumor at **case 1:** (0,0,0.6) and **case 2:** (0.183,0.213,0.586). In these two cases, the influence of the tumor on each electrode E_l in terms of center potential u_l and current density J_l of (1b) is shown in Table 2. Compared with the results in case 2, the electrode currents in case 1 show symmetric patterns with respect to the z-axis when the tumor is at (0,0,0.6), consistent with the system setting. Meanwhile, the tumor can be found to have the most impact on the electrode E_1 among the eight electrodes. In case 1, the relative difference of current density J_1 over E_1 is 3.745% and the relative difference of the potential u_1 at (0,0,1) is -13.267%. While in case 2, when the tumor is close to both E_1 and E_2, the difference of the electrode currents J_1 and J_2 is more obvious than that which on other electrodes. The potentials over E_1 and E_2 with or without a tumor in these two cases calculated by BEM illustrate a visible difference especially in the central region (refer to the contour Fig. 11 and Fig. 12).

Table 2
Center potential u_l and current density J_l on each electrode E_l by BEM.

E_l	no tumor		with tumor (case 1)				with tumor (case 2)			
	u_l	J_l	u_l	J_l	$d(u_l)$	$d(J_l)$	u_l	J_l	$d(u_l)$	$d(J_l)$
E_1	0.233058	1.344907	0.202139	1.395272	-13.267%	3.745%	0.220476	1.369742	-5.399%	1.847%
E_2	-0.274693	-1.403436	-0.271830	-1.409190	-1.042%	0.410%	-0.264733	-1.423535	-3.626%	1.432%
E_3	0.247192	1.462005	0.250982	1.453928	1.533%	-0.552%	0.250304	1.455330	1.259%	-0.457%
E_4	-0.274693	-1.403436	-0.271031	-1.411251	-1.333%	0.557%	-0.273258	-1.406504	-0.522%	0.219%
E_5	0.233058	1.344907	0.236666	1.337196	1.548%	-0.573%	0.233775	1.343370	0.308%	-0.114%
E_6	-0.274693	-1.403436	-0.271031	-1.411251	-1.333%	0.557%	-0.274522	-1.403797	-0.062%	0.026%
E_7	0.247192	1.462005	0.250983	1.453928	1.534%	-0.552%	0.246626	1.463222	-0.229%	0.083%
E_8	-0.274693	-1.403436	-0.271830	-1.409190	-1.042%	0.410%	-0.277192	-1.398048	0.910%	-0.384%
overall	-	0.000010	-	-0.000070	-	-	-	-0.000027	-	-

$d(\cdot)$ means the difference with and without tumor.

(a) potential of the center of E_1 (no tumor).   (b) potential of the center of E_2 (no tumor).

Fig. 9. Convergence of potential in terms of NP in the case without tumor (The red horizontal line is the reference value by BEM).

5. PMIC solution for EIT and computational cost

The PIMC method proposed in Section 3.5 will be used to compute the potential and current density over electrodes for the situations with or without tumor presence in the media and two cases of tumor locations as in Section 4.3 will be considered. The program runs on 8 Intel(R) Xeon(R) CPU E7-8837 with 8 cores in each CPU.

The convergence of PIMC method. The number of Monte Carlo simulations N is set to be $2e5$ for all the mesh points on the electrodes. The length of path NP is $5e5$ for the case without the tumor and $4e5$ for the cases with the tumor. A discussion about the value of NP is presented below. The step size of the WOS inside the ϵ-region near the reflecting boundary Δx is set to be $5e-4$, the width of the ϵ-region of the reflecting boundary $\epsilon_{\text{reflecting}} = 1.4\Delta x$, and the width of the absorption ϵ-shell of the absorbing boundary (i.e., boundary of the tumor) $\epsilon_{\text{absorbing}} = 1e-5$. We expect that for large enough N, as NP increases, the simulation result will approach the true (reference) value. To illustrate this, we show the relation between the result and NP in Fig. 9 and Fig. 10.

In our experiments, the criteria for path length truncation NP are that the results stabilize. If the tumor is included inside, it is easy to decide when to truncate. Due to the absorbing nature of the tumor, all paths will eventually be absorbed by the tumor in theory. The path truncation standard is that over 99% of the path have been absorbed. When NP is set to be $4e5$, the rate of absorption of the paths starting from the point furthest from the tumor $(0, 0, -1)$ reaches 99.6%, more than enough to meet this requirement. However, if there is no tumor inside the object, the paths will keep walking inside the domain. Since the contribution of the Neumann part is zero, the forward EIT problem without the tumor can be regarded as a Robin problem. For the Robin problem, due to the existence of the factor $\hat{e}_c(t)$ inside the integrand, when the length of the path is long enough, the impact of the subsequent collisions on the integral can be ignored. Our numerical experiments found that the local time $L(t)$ is proportional to NP with a proportional constant of $1.2 * \frac{(\Delta x)^2}{3\epsilon}$. Therefore, it can be estimated from this relationship how large NP should be when the factor reaches one-thousandth or even smaller. In addition, considering that the ratio of Robin boundary area to Neumann boundary area in this problem is 1:11.35, the value of NP needs to be about 12 times the value for an all Robin problem. Obviously, this is a rough heuristic estimate and can only serve as a guide. If a more accurate truncation is needed, dynamic monitoring of the functional $\hat{e}_c(t)$ can be used. Calculating the value of the functional in real-time when paths are walking can make the truncation more accurate, but may incur certain computational cost.
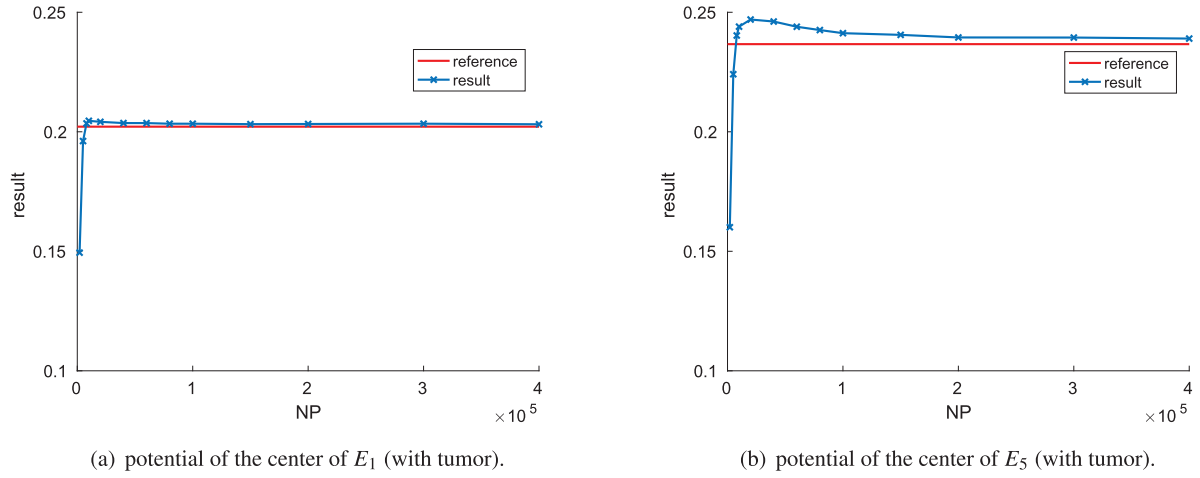
(a) potential of the center of E_1 (with tumor).

(b) potential of the center of E_5 (with tumor).

Fig. 10. Convergence of potential in terms of NP in case 1 with tumor (The red horizontal line is the reference value by BEM).

Table 3
The center potentials u_l on each electrode E_l by BEM and PIMC.

E_l	no tumor			with tumor (case 1)			with tumor (case 2)		
	BEM	$PIMC$	error	BEM	$PIMC$	error	BEM	$PIMC$	error
E_1	0.233058	0.230452	-1.118%	0.202139	0.203124	0.487%	0.220476	0.221358	0.400%
E_2	-0.274693	-0.274986	0.107%	-0.271830	-0.271031	-0.294%	-0.264733	-0.263345	-0.524%
E_3	0.247192	0.246814	-0.153%	0.250982	0.253320	0.932%	0.250304	0.253005	1.079%
E_4	-0.274693	-0.277815	1.137%	-0.271031	-0.273285	0.832%	-0.273258	-0.275570	0.846%
E_5	0.233058	0.231721	-0.574%	0.236666	0.239001	0.987%	0.233775	0.235188	0.604%
E_6	-0.274693	-0.274991	0.108%	-0.271031	-0.272008	0.360%	-0.274522	-0.275177	0.239%
E_7	0.247192	0.245973	-0.493%	0.250983	0.250056	-0.369%	0.246626	0.246027	-0.243%
E_8	-0.274693	-0.275193	0.182%	-0.271830	-0.272189	0.132%	-0.277192	-0.277985	0.286%

During the random walk simulation, the specific value of the constant potential on the tumor u_0 is unknown. However, the potential u approximated by PIMC method can be written as a sum

$$u = u' + \alpha u_0, \tag{34}$$

where u' is the sum of the first two terms in formula (26), and α is the average of the final functional $\hat{e}_c(\tau_{\Gamma_1})$ calculated by Monte Carlo simulations. According to equation (1b) and equation (1e), we can get an expression of total current (zero) on the electrodes, from which the value of constant u_0 can be determined by

$$\sum_{l=1}^{8} \int_{E_l} (\phi_3(x) + c(u' + \alpha u_0)) dS = 0, \tag{35}$$

i.e.,

$$u_0 = -\frac{\sum_{l=1}^{8} \int_{E_l} (\phi_3(x) + cu') dS}{c \sum_{l=1}^{8} \int_{E_l} \alpha dS}. \tag{36}$$

The calculated u_0 in case 1 and case 2 equal 0.001016 and -0.015345, respectively.

The accuracy of PIMC method. The center potential u_l over each electrode E_l obtained by PIMC method is shown in Table 3, compared with the BEM result. As seen from the table, the relative errors of the potentials between the PIMC results and the reference values remain at a low 1% level, which validates the PIMC method. Fig. 11 and Fig. 12 show potentials over E_1 and E_2 with or without the tumor obtained by polynomial interpolation of the PIMC results only on a 3×3 mesh on each electrode. The potentials along the equator directly calculated from sampling points on E_1 and E_2 are presented in Fig. 13, showing the difference more clearly. With the numerical approximations of potentials on the boundary, the Neumann values can be found from (2b), and the current from (1b) by evaluating the integral of the Neumann data with Gauss quadratures, thus, the voltage-to-current map can been achieved. The current densities J_l obtained through the 3×3 meshes are shown in Table 4 with good accuracy and most of the relative errors are within 0.5%.
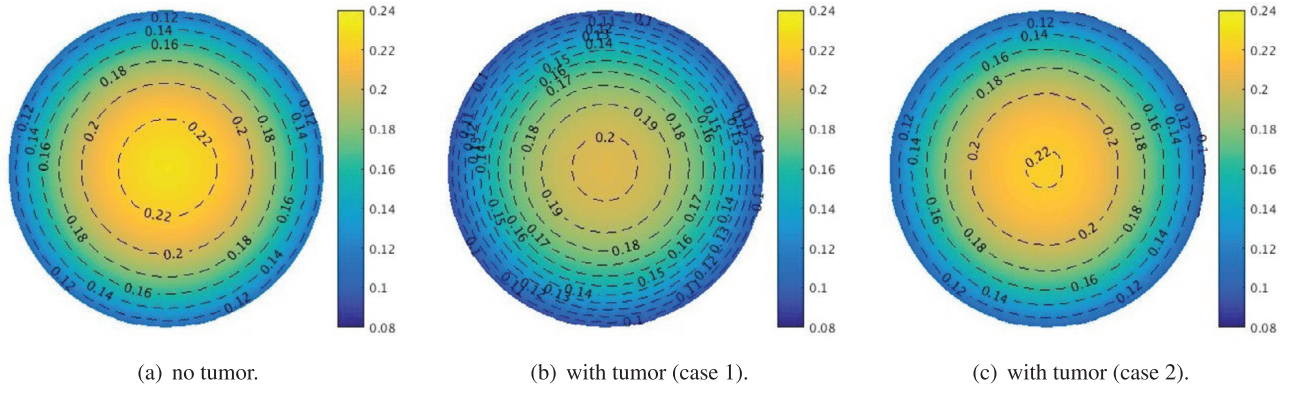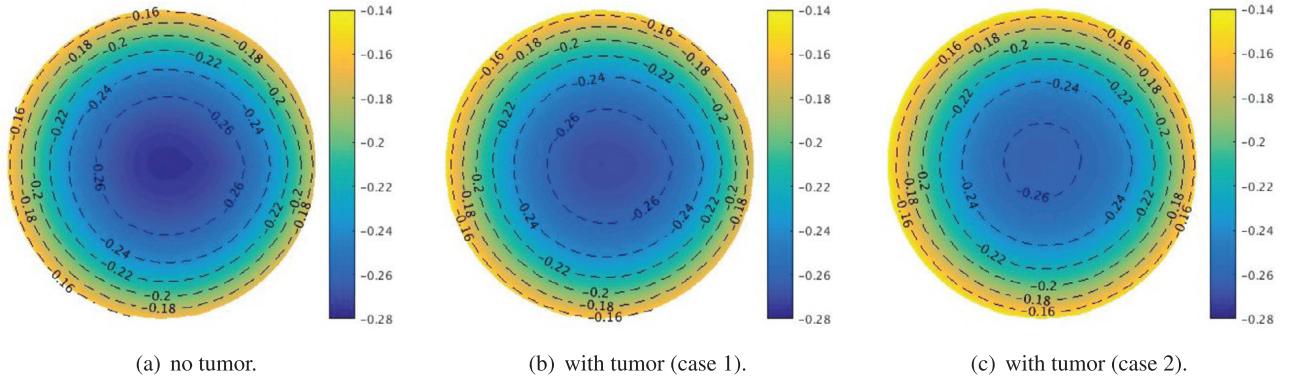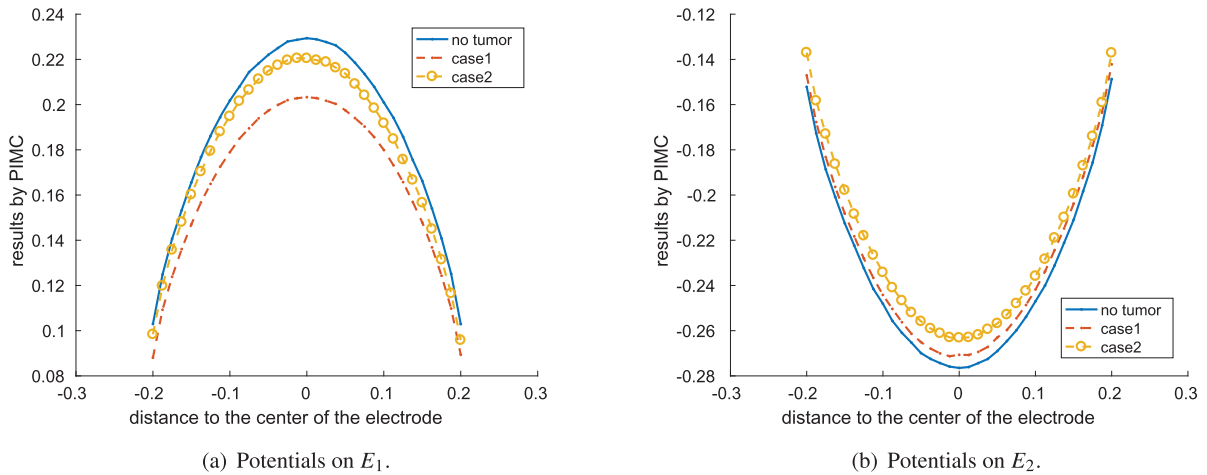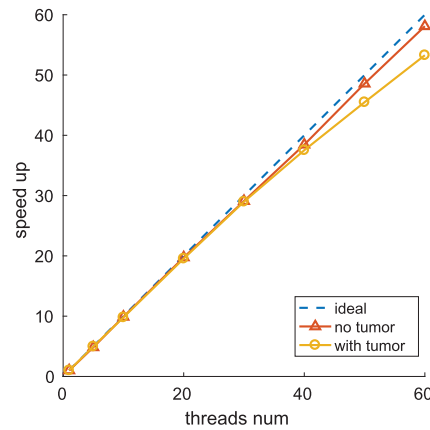
(a) no tumor.   (b) with tumor (case 1).   (c) with tumor (case 2).

Fig. 11. Potentials on E_1 by PIMC.

(a) no tumor.   (b) with tumor (case 1).   (c) with tumor (case 2).

Fig. 12. Potentials on E_2 by PIMC.

(a) Potentials on E_1.   (b) Potentials on E_2.

Fig. 13. Potentials along the equator on the electrodes.

The parallelism of PIMC method. Because of the high independence of sampling paths, PIMC method possesses excellent intrinsic parallel efficiency just using the simple OpenMP API [21] as shown in Fig. 14. We can see that when the number of threads increases from 1 to 60, the speedup of PIMC method maintains an almost ideal linear growth. When the number of threads is set as 60, the corresponding speedups are 53.282 and 58.090 with or without tumor. The reason for the minor difference in speedups is that the sampling paths with different lengths due to the Dirichlet boundary of the tumor are forced to synchronize by the implicit barrier of OpenMP. In contrast, it is difficult to parallelize solving the linear system of the BEM method. Although The BEM method can maintain about 90% parallel efficiency on 10 nodes, the parallel efficiency drops sharply to 44% with more than 60 nodes [9]. This will cause difficulties for the BEM method when the scale of equations becomes too large. In general, PIMC method possesses great advantages in large-scale parallel computing and can make full use of multi-core processors without inter-core communication due to the natural parallelism.

Table 4

The current density J_l on each electrode E_l by BEM and PIMC.

E_l	no tumor			with tumor (case 1)			with tumor (case 2)		
	BEM	*PIMC*	*error*	*BEM*	*PIMC*	*error*	*BEM*	*PIMC*	*error*
E_1	1.344907	1.348172	0.243%	1.395272	1.388235	-0.504%	1.369742	1.362972	-0.494%
E_2	-1.403436	-1.399544	-0.277%	-1.409190	-1.407617	-0.112%	-1.423535	-1.422568	-0.068%
E_3	1.462005	1.451656	-0.708%	1.453928	1.446767	-0.493%	1.455330	1.448050	-0.500%
E_4	-1.403436	-1.398606	-0.344%	-1.411251	-1.403249	-0.567%	-1.406504	-1.397586	-0.634%
E_5	1.344907	1.348858	0.294%	1.337196	1.331359	-0.437%	1.343370	1.338448	-0.366%
E_6	-1.403436	-1.409004	0.397%	-1.411251	-1.404332	-0.490%	-1.403797	-1.397492	-0.449%
E_7	1.462005	1.455570	-0.440%	1.453928	1.453032	-0.062%	1.463222	1.460978	-0.153%
E_8	-1.403436	-1.392665	-0.767%	-1.409190	-1.404195	-0.354%	-1.398048	-1.392803	-0.375%
overall	0.000010	0.004437	-	-0.000070	0.000000	-	-0.000027	0.000000	-

Fig. 14. The parallelism of PIMC method.

Table 5

Computational time cost.

	size	*time* (s)[1]	*time* (s)[2]	*total time* (s)	*average time per mesh point* (s)
BEM	80330	26634	1242	27876	0.347
PIMC	80	-	-	5103	63.788

[1] the time for building the boundary integral equation.
[2] the time for solving the boundary integral equation.

The computational cost of PIMC method. Although the average time of BEM per mesh point seems to be less, the proposed PIMC method has a about 5.46× speedup in calculating the current densities of the eight electrodes. Table 5 lists the time taken to calculate the current densities across the eight electrodes. It takes about 28,000 s for BEM to build and solve an equation with 80,330 mesh points, of which 12,968 points are on the electrodes, while the PIMC method requires 20 s-85 s (mean 63.788 s) to calculate the potential at one point (depends on the distance from the tumor). 60 threads are used in parallel to build the equations in BEM and simulate the random walk of the paths in the PIMC method. Since our standard for truncating NP in the PIMC method is for the result to stabilize, the calculation time of PIMC is relatively long, especially in the case without the tumor where the paths keep walking before truncation.

However, the proposed method provides a very effective method to solve a single-point problem in field analysis. Correspondingly, if BEM is used to solve the single-point problem, it is necessary to build a global mesh and solve a large global matrix. If only potentials at several points such as the electrode centers are needed, the time cost used by the PIMC method will be much smaller than that required by the BEM.

In addition, in our calculations, the contact impedance z_l is taken to be 0.5 while it can be very close to zero in practice. It should be noted that the regularity of potential u decreases as the contact impedance approaches zero [18], which becomes a huge hindrance to accurate numerical resolution as in practice usually good contacts with small contact impedance are used. In that case, the voltages will jump drastically and then a denser mesh for the BEM must be required at the contacts to avoid large errors in the voltages. On the other hand, the PIMC will not be affected as each point is independently calculated.

Finally, in terms of the difficulty of programming, the code implementation of the proposed PIMC method is straightforward. Compared with a large amount of matrix entry calculation in the BEM method, the implementation of the WOS

method is much simpler and not prone to coding errors. When the geometry of the domain in 3-D is complicated or boundary integral equation is difficult to solve, the PIMC method will be a preferred method to use.

6. Conclusions and future work

This paper presents a path integral Monte Carlo method to solve the forward problem of EIT and the voltage-to-current map for iterative algorithms of the inverse EIT problem where a forward problem needs to be solved at each iteration. The method is intrinsically parallel and potentials and currents can be calculated simultaneously at different electrodes, independently. The ill-posedness of the inverse problem requires high accuracy of the forward solver, otherwise it may lead to large errors in the reconstruction of conductivity. The PIMC method is accurate enough and is preferred over traditional boundary element or finite element methods when solution only on the electrodes is needed.

In a broader sense, the PIMC method can give single-point field analysis problem with the mixed boundary conditions. Solving the single-point problem directly and quickly is an advantage of the method over global deterministic algorithms. Moreover, the PIMC method is not only suitable for electric field analysis, but also for other field analysis problems, which will be considered for future work. To further improve the efficiency of the PIMC method, importance sampling of paths will also be investigated by using a prior estimate of the hitting probability of the Brownian paths in terms of the location and geometry of the boundary [25].

CRediT authorship contribution statement

Cuiyang Ding: Conceptualization, Methodology, Software, Writing – original draft. **Yijing Zhou:** Conceptualization, Methodology, Software, Writing – original draft. **Wei Cai:** Conceptualization, Formal analysis, Funding acquisition, Methodology, Supervision, Writing – review & editing. **Xuan Zeng:** Funding acquisition, Methodology, Supervision, Writing – review & editing. **Changhao Yan:** Funding acquisition, Methodology, Supervision, Writing – review & editing.

Declaration of competing interest

The authors declare that they have no known competing financial interests or personal relationships that could have appeared to influence the work reported in this paper.

Data availability

No data was used for the research described in the article.

Acknowledgement

References

[1] G. Alessandrini, Stable determination of conductivity by boundary measurements, Appl. Anal. 27 (1–3) (1988) 153–172.
[2] L. Borcea, Electrical impedance tomography, Inverse Probl. 18 (6) (2002) R99.
[3] A. Borsic, B.M. Graham, A. Adler, W.R.B. Lionheart, Total variation regularization in electrical impedance tomography, 2007.
[4] A.P. Calderón, On an inverse boundary value problem, Comput. Appl. Math. 25 (2–3) (2006) 133–138.
[5] M. Cheney Margaret, D. Isaacson, Jonathan C. Newell, Electrical impedance tomography, SIAM Rev. 41 (1) (1999) 85–101.
[6] K.L. Chung Green, Brown, and Probability and Brownian Motion on the Line, World Scientific Pub Co Inc, 2002.
[7] J.F. Douglas, Integral equation approach to condensed matter relaxation, J. Phys. Condens. Matter 11 (10A) (1999) A329.
[8] J.A. Given, C. Hwang, M. Mascagni, First- and last-passage Monte Carlo algorithms for the charge density distribution on a conducting surface, Phys. Rev. E 66 (2002) 056704.
[9] Y. Hsiao, L. Daniel, CAPLET: a highly parallelized field solver for capacitance extraction using instantiable basis functions, IEEE Trans. Comput.-Aided Des. Integr. Circuits Syst. 35 (3) (2015) 458–470.
[10] (Elton) P. Hsu, Reflecting Brownian motion, boundary local time and the Neumann problem, Diss. Abstr. Int., B. Sci. Eng 45 (6) (1984).
[11] J.P. Kaipio, V. Kolehmainen, E. Somersalo, M. Vauhkonen, Statistical inversion and Monte Carlo sampling methods in electrical impedance tomography, Inverse Probl. 16 (5) (2000) 1487.
[12] I. Karatzas, S.E. Shreve, Brownian Motion and Stochastic Calculus, Springer-Verlag New York Inc., 1988.
[13] R. Kohn, M. Vogelius, Determining conductivity by boundary measurements, Commun. Pure Appl. Math. 37 (1984) 113–123.
[14] P. Lévy, Processus Stochastiques et Mouvement Brownien, Gauthier-Villars, Paris, 1948.
[15] H.M. Lin, H.Z. Tang, W. Cai, Accuracy and efficiency in computing electrostatic potential for an ion channel model in layered dielectric/electrolyte media, J. Comput. Phys. 259 (2014) 488–512.
[16] P.L. Lions, A.S. Sznitman, Stochastic differential equations with reflecting boundary conditions, Commun. Pure Appl. Math. 37 (4) (1984) 511–537.
[17] S. Maire, E. Tanré, Monte Carlo approximations of the Neumann problem, Monte Carlo Methods Appl. 19 (3) (2013 Oct 1) 201–236.
[18] S. Maire, M. Simon, A partially reflecting random walk on spheres algorithm for electrical impedance tomography, J. Comput. Phys. 303 (2015) 413–430.
[19] J.P. Morillon, Numerical solutions of linear mixed boundary value problems using stochastic representations, Int. J. Numer. Methods Eng. 40 (1997) 387–405.

[20] M.E. Müller, Some continuous Monte Carlo methods for the Dirichlet problem, Ann. Math. Stat. 27 (3) (1956) 569–589.

[21] OpenMP, The OpenMP API specification for parallel programming, https://www.openmp.org/.

[22] V.G. Papanicolaou, The probabilistic solution of the third boundary value problem for second order elliptic equations, Probab. Theory Relat. Fields 87 (1990) 27–77.

[23] K.K. Sabelfeld, D. Talay, Integral formulation of the boundary value problems and the method of random walk on spheres, Monte Carlo Methods Appl. 1 (1995) 1–34.

[24] F. Santosa, M. Vogelius, A backprojection algorithm for electrical impedance imaging, SIAM J. Appl. Math. (1990) 216–243.

[25] Z. Schuss, Brownian Dynamics at Boundaries and Interfaces, Springer-Verlag, New York, 2015.

[26] N.A. Simonov, Walk-on-spheres algorithm for solving third boundary value problem, Appl. Math. Lett. 64 (2017) 156–161.

[27] A.V. Skorokhod, Stochastic equations for diffusion processes in a bounded region, Theory Probab. Appl. 6 (3) (1961) 264–274.

[28] E. Somersalo, M. Cheney, D. Isaacson, Existence and uniqueness for electrode models for electric current computed tomography, SIAM J. Appl. Math. 52 (4) (1992) 1023–1040.

[29] J. Sylvester, G. Uhlmann, A uniqueness theorem for an inverse boundary value problem in electrical prospection, Commun. Pure Appl. Math. 39 (1986) 91–112.

[30] H. Tanaka, Stochastic differential equations with reflecting boundary condition in convex regions, Hiroshima Math. J. 9 (1) (1979) 163–177.

[31] M. Vauhkonen, et al., Tikhonov regularization and prior information in electrical impedance tomography, IEEE Trans. Med. Imaging 17 (2) (1998) 285–293.

[32] C. Yan, W. Cai, X. Zeng, A parallel method for solving Laplace equations with Dirichlet data using local boundary integral equations and random walks, SIAM J. Sci. Comput. 35 (2013) B868–B889.

[33] Y. Zhou, W. Cai, Numerical solution of the Robin problem of Laplace equations with a Feynman-Kac formula and reflecting Brownian motions, J. Sci. Comput. 69 (1) (2016) 107–121.

[34] Y. Zhou, W. Cai, (Elton) P. Hsu, Computation of local time of reflecting Brownian motion and probabilistic representation of the Neumann problem, Commun. Math. Sci. 15 (2017) 237–259.